Polarized and narrow excitonic emission from graphene-capped monolayer WS$_2$ through resonant phonon relaxation

Garima Gupta and Kausik Majumdar [*]

Department of Electrical Communication Engineering, Indian Institute of Science, Bangalore 560012, India

The broadening and polarization of excitonic luminescence in monolayer transition metal dichalcogenides largely suffer from inhomogeneity and temperature – an unresolved problem to date. In this work, through few-layer graphene encapsulation of monolayer WS$_2$, we reduce the interexcitonic energy separation, which then can have a narrow resonance with a specific phonon mode of our choice. The resulting single-step exciton relaxation with the resonating phonon mode significantly suppresses the inhomogeneous broadening, allowing us to achieve the narrowest exciton linewidth of 1.06 meV (which translates to 0.19 meV after deconvolution with the excitation laser linewidth). The single-phonon resonance helps to achieve a high quantum efficiency despite graphene encapsulation. The technique is powerful in tuning the exciton polarization during relaxation by choosing a specific resonating phonon mode. For example, the valley coherence (polarization) improves from $\sim$68%($\sim$40%) to $\sim$90% ($\sim$75%) on resonance with $2A_1^{'}$ and $A_1^{'}$ modes, respectively. We further demonstrate a strong polarization reversal on resonance with a chiral phonon mode. Strikingly, the above features remain robust against temperature (up to 200 K) and sample age (a few months in ambient condition). The findings will lead to clean excitonic measurements without requiring cryogenic cooling.

I. INTRODUCTION

Despite being ultrathin, the monolayers of transition metal dichalcogenides (TMDs) are highly luminescent because of the strongly bound two-dimensional (2D) excitons [1–4]. However, it is practically impossible to avoid the influence of the surrounding environment on the monolayers [5], obscuring the innate excitonic features [6]. The presence of potential fluctuations from external (adsorbed or substrate charge impurities) [7] and internal (defects) [8–11] factors leads to a large inhomogeneous broadening of the photoluminescence (PL) peaks [12]. Several methods, such as chemical treatment of the substrate [13] and encapsulation with hBN [14–17] or graphene [18] flakes, have been explored to reduce the inhomogeneous broadening. Encapsulation with graphene does not just screen the substrate induced inhomogeneity, but also suppresses emission from other excitonic species such as defect bound excitons, trions, and charged biexcitons [18]. Additionally, it also helps in retaining a high valley coherence and valley polarization of the excitons due to suppression of the electron-hole exchange interaction [19]. However, one drawback of this technique is reduced quantum efficiency and hence weak peak intensity due to fast carrier transfer to graphene during the relaxation process. In addition, the applicability of all these techniques is largely limited to cryogenic temperatures only. The room temperature PL inevitably suffers from broad linewidth and negligible exciton polarization. Hence, it remains a challenge to achieve narrow-linewidth, highly polarized exciton peaks at room temperature.

In this work, we overcome these issues by using a simple technique: (a) We sandwich a monolayer WS$_2$ between two few-layer graphene (FLG) flakes such that the resulting screening makes the interexcitonic energy separation (Δ_{ns-1s}; $n > 1$) approximately equal to an optical phonon energy in the system. (b) Using a tunable laser, we resonantly generate the higher energy excitons (ns), which undergo ultrafast relaxation to the lowest energy $1s$ state in a single step, by scattering with the resonating phonon mode. As an outcome of this technique, we achieve a (1) high intensity, (2) ultranarrow-linewidth (1.06 meV) exciton peak which also shows (3) a high valley coherence measured by the degree of linear polarization (DOLP $\sim$90%) and valley polarization measured by the degree of circular polarization (DOCP $\sim$ 75%). These features remain robust until 200 K, making this technique appealing for several experiments and applications.

II. VARIOUS MECHANISMS OF RELAXATION

To understand the working principle of this technique, let us revisit the process of exciton generation, relaxation, and light emission from radiative recombination. Initially, the higher energy excitons inside the light cone of the ns band, that resonate with the incoming photon energy (hc/λ_{ex}), are generated (Fig. 1). These excitons can relax to the $1s$ band through a combination of the following mechanisms: M1 – losing energy through multiple scatterings with various phonon modes in the system [Fig. 1(a)], M2 – through direct optical transition by photon emission between the dipole-coupled Rydberg states [Fig. 1(b)], and M3 – as explored in this paper as a special case of M1 – by scattering with a single resonating zone center optical phonon mode and relaxing to
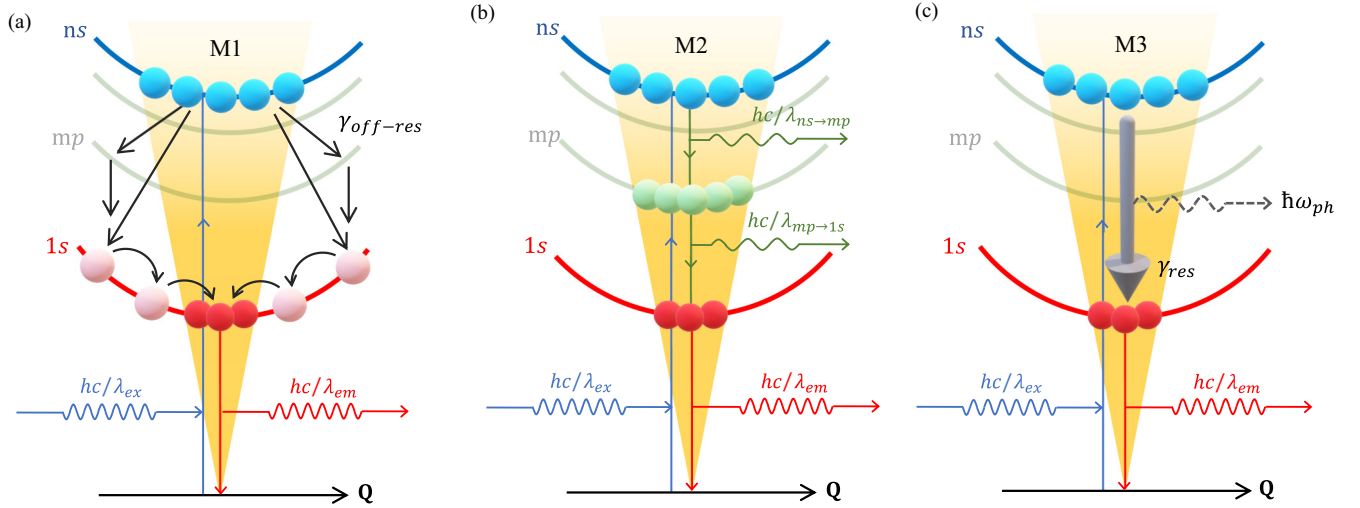
*kausikm@iisc.ac.in

FIG. 1. Exciton relaxation mechanisms: Photons of energy hc/λ_{ex} excite higher energy excitons inside the light cone of an ns exciton band. These excitons can relax to the lowest energy $1s$ band in the following three ways: (a) M1–through scattering with multiple phonons, (b) M2–radiative transition through photon emission between the dipole-coupled Rydberg states, and (c) M3–in a single step by scattering with a resonating phonon mode of energy $\hbar\omega_{ph}(=\Delta_{ns-1s})$. Finally, the $1s$ excitons inside the light cone radiatively recombine and emit a photon of energy hc/λ_{em}.

the $1s$ state in one step [Fig. 1(c)]. Finally, the excitons inside the light cone of the $1s$ band recombine radiatively to emit light of energy hc/λ_{em}. Due to both incoming and outgoing resonance, we expect this single-step scattering to dominate the $ns \rightarrow 1s$ transition. The implications of this single-step relaxation on emission are discussed in the upcoming sections.

III. EXPERIMENTAL OBSERVATIONS

The emission spectrum of the FLG-WS$_2$-FLG (GWG) stack [Fig. 2(a)] (see Methods for sample preparation) taken with 532 nm laser excitation at 5 K shows conspicuous $1s$ and $2s$ exciton peaks [Fig. 2(b)], with the $1s$ peak exhibiting an average linewidth of ~9.5 meV (inset). Due to the FLG induced screening, we obtain $\Delta_{2s-1s} \sim 31.5$ meV, which matches well with the previously reported value [20] and implies a significant reduction in the exciton binding energy. The large redshift of the higher energy exciton states [21] brings the interexcitonic separation in the regime of optical phonon energies.

We carry out the photoluminescence excitation (PLE) spectroscopy of this GWG stack and monitor emission from the $1s$ state. The excitation wavelength is tuned from 570 to 600 nm using a supercontinuum laser source and a monochromator setup (see Methods for measurement details). Figure 2(c) (left panel) shows the color plot of the $1s$ intensity (in log scale) as a function of λ_{ex} and λ_{em}. The corresponding intensity color plot (in linear scale), normalized at each λ_{ex}, is shown in the right panel. At specific values of λ_{ex}, where the resonance condition $\Delta_{ns-1s} \approx \hbar\omega_{ph}$ is satisfied, we observe highly luminescent and narrow-linewidth exciton peaks through mechanism M3 (see Supplemental Material [22] for individual spectrum). The resonating phonon modes are labeled in Fig. 2(c) [23,24]. The line cuts show the individual spectrum in Figs. 2(d)–2(f). The broad pink back-

grounds represent emission from excitons formed through multiphonon relaxation process (M1). The sharp green peaks in Figs. 2(d) and 2(e) correspond to excitons formed through single-phonon (M3) and two-phonon resonance, respectively. The exciton peak at single- (two-) phonon resonance is remarkably narrow and about 124-fold (3.4-fold) enhanced [Figs. 2(d) and 2(e)], as compared to the broad and weakly luminescent exciton peak in Fig. 2(f), when such resonance is absent.

IV. REDUCTION IN THE INHOMOGENEOUS LINEWIDTH

External and internal inhomogeneities cause potential fluctuations in the monolayer. The resulting random doping and stark effect lead to a spatial perturbation in the exciton peak position [Fig. 3(a)]. This leads to a real space to energy mapping of the excitons. The intersections of the solid lines with the spatial exciton energy distribution in the top panel of Fig. 3(a) are the equienergy spots corresponding to a specific exciton energy in the real space. The bottom inset of Fig. 3(b) schematically shows such equienergy locations under the laser spot at different $1s$ exciton energies. The inhomogeneous broadening is a result of collecting photons from all such spatially distributed $1s$ states under the laser spot [Fig. 3(b) and left panel of Fig. 3(c)].

The proposed technique relies on exploiting the narrow spectral resonance between the incoming excitation and a specific $1s$ exciton energy state via scattering with the resonating phonon mode [Fig. 3(b) and right panel of Fig. 3(c)]. To explain this, let us look closely into the case when A'_1 (418 cm^{-1}) is the resonating phonon mode in the relaxation process for $589 \leqslant \lambda_{ex} \leqslant 600$ nm. As estimated from the Bethe-Salpeter equation, λ_{ex} in this range generates excitons in the bands in the range $6s \leqslant ns \leqslant 3s$ (see Note S1 in Supplemental Material [22]). On the excitation side, only the energy states in the inhomogeneously broadened ns exciton band that resonate in
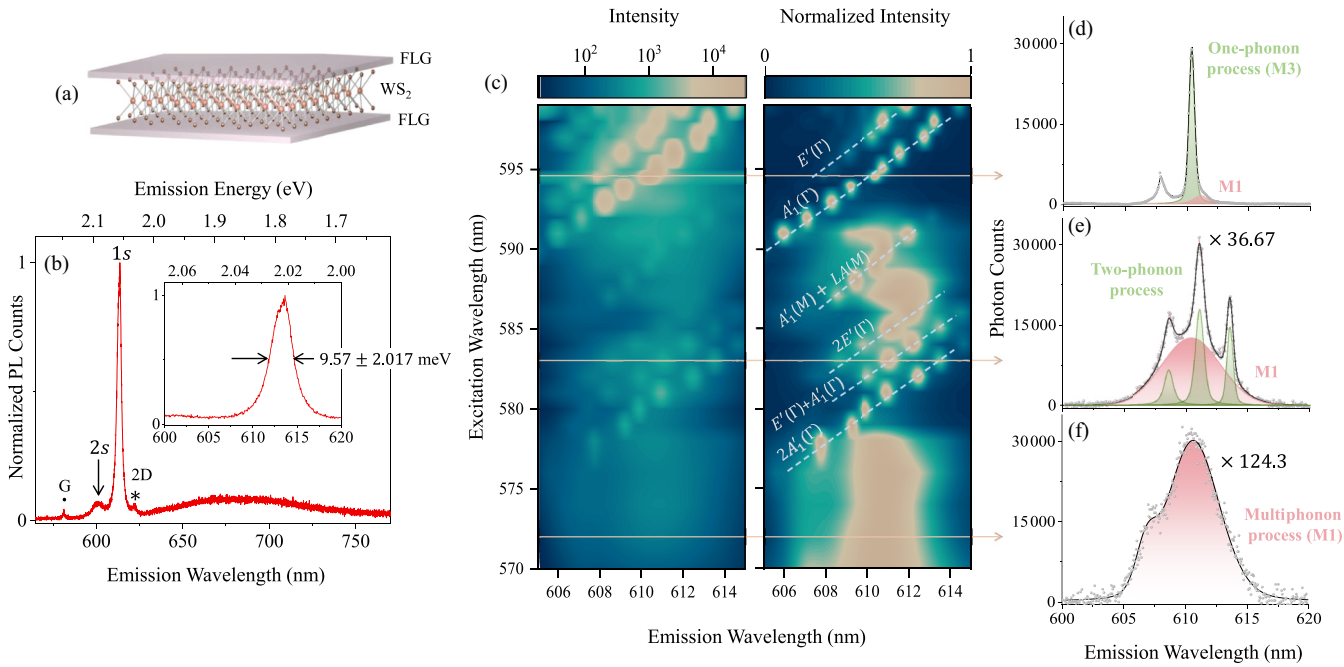
FIG. 2. Excitation spectroscopy on GWG sample: (a) Schematic representation of the GWG stack. (b) PL spectrum at 5 K taken with 532 nm excitation on the stack. The PL shows the $1s$ and $2s$ exciton peak from monolayer WS_2, apart from the 2D (*) and G (•) Raman mode from the encapsulating FLG flakes. Inset: Linewidth of the $1s$ exciton peak (9.57 ± 2.017 meV) obtained with off-resonant excitation. (c) Left panel: Color plot of the excitation spectroscopy measurement showing the $1s$ exciton emission intensity (in log scale) as a function of the emission and excitation wavelength. Right panel: The intensity (in linear scale) normalized at each excitation wavelength. The resonating phonon modes are labeled. The line cuts showing the emission spectrum at (d) 594.5, (e) 583, and (f) 572 nm excitation are plotted to distinguish the emission from single-step relaxation M3 [green shaded curves in (d)] and two-step relaxation [green shaded curves in (e)] from multiple-step relaxation M1 [pink shaded curves in (d)–(f)].

energy with hc/λ_{ex} are excited [green laser spikes, Fig. 3(b)]. Thus, the incoming laser performs a preliminary spectral (and hence spatial) filtering by generating excitons at the ns state at specific locations in the real space. Further, as Δ_{ns-1s} (≈ 52 meV) is around the energy of the A_1' phonon mode in WS_2, relaxation to the $1s$ state is dominated by scattering with the A_1' phonons in a single step through mechanism M3 [dashed arrows, Fig. 3(b)]. As this relaxation process is ultrafast, only those $1s$ energy states in the inhomogeneously broadened peak, that lie at an energy $\hbar\omega_{A_{1g}}$ below hc/λ_{ex}, are populated [solid red spikes, Fig. 3(b)]. This leaves little chance for populating the other states in the distribution through slow, multiphonon relaxation mechanisms (such as M1), thus truncating the inhomogeneous broadening significantly. This implies that we are essentially collecting light only from the equienergy spots in the real space that correspond to those resonating $1s$ states.

The experimental demonstration of the above mechanism showing light emission from the specifically populated resonant $1s$ states is shown in Fig. 3(d). As we tune λ_{ex}, different regions of the inhomogeneously distributed $1s$ states satisfying $\Delta_{ns-1s} \approx \hbar\omega_{A_1'}$ are populated and emit light (shaded orange peaks). For comparison, we also plot the inhomogeneously broadened envelope obtained at $\lambda_{ex} = 532$ nm (in gray), which is a collective outcome of emission from all these individual peaks in the distribution (through M1). This shows the supremacy of our technique, which makes excitonic emission much less sensitive to the surrounding inhomogene-

ity. This is also evident from the invariance of the emission linewidth of individual peaks (see Fig. S4 in Supplemental Material [22]). The result from another GWG sample is shown in Fig. S5 of Supplemental Material [22].

To support the argument, we perform the emission imaging with 591, 593, and 595 nm excitation wavelengths in Fig. 3(e). We observe a significant modulation in the spatial distribution of the luminescence peaks [marked by arrows in Fig. 3(d)], suggesting varying spatial profiles of the different equienergy spots.

We obtain an average total linewidth of 1.21 ± 0.04 meV [Fig. 3(f) for a representative plot], with the lowest linewidth being 1.06 meV (see Fig. S6 in Supplemental Material [22]). These numbers are low compared to other linewidths reported from free excitons in TMDC monolayers [13,14,16,25,26]. Please note that the difference between the laser linewidth (~ 0.8 meV) and the narrowest obtained exciton linewidth is well above our system resolution of $\sim 40-60$ µeV. On deconvoluting with the excitation laser having nonzero broadening, we extract an exciton linewidth of $\sim 0.19 \pm 0.07$ meV, which denotes an upper bound on the homogeneous broadening of the $1s$ exciton states in the GWG stack. This implies a net exciton lifetime $\geqslant 1.65$ ps in the system. This timescale is in good agreement with the reported lifetime values obtained from time resolved PL measurements [18,27]. We report here the achievement of an excitonic emission linewidth down to the true homogeneous limit. Due to suppressed inhomogeneity, we also observe a tighter distribution of the linewidth with
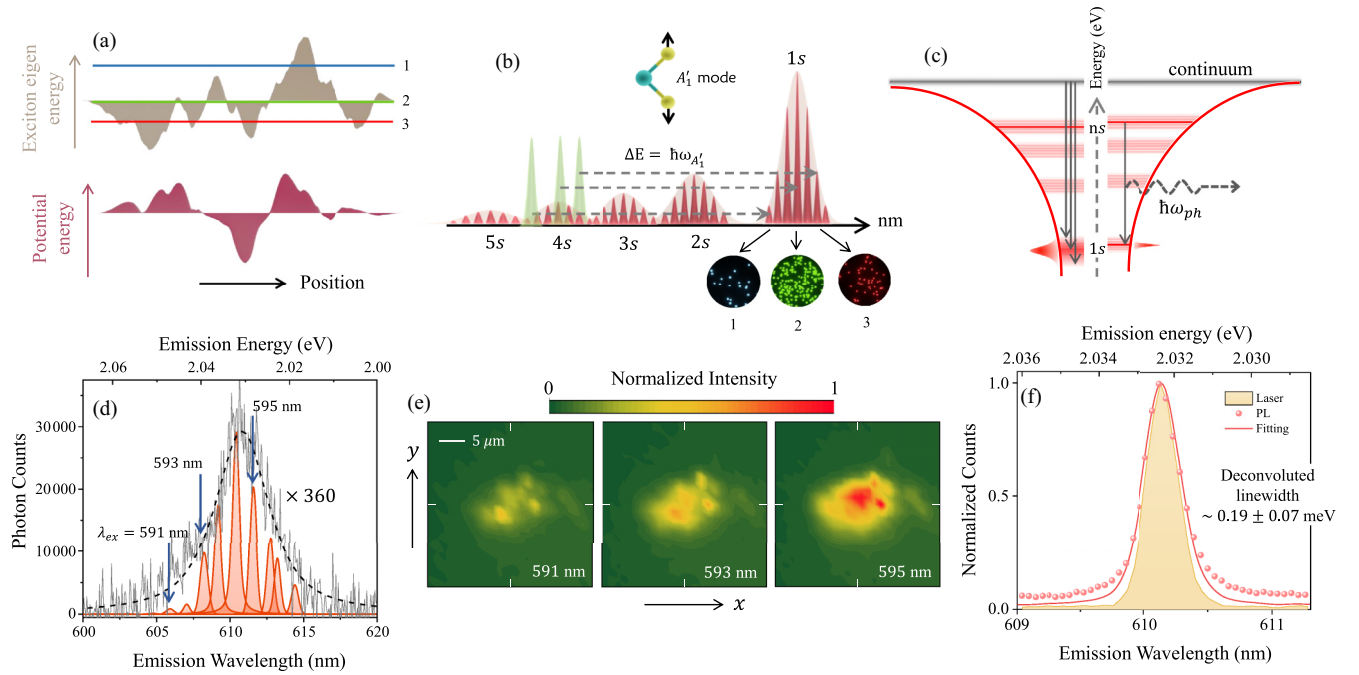
FIG. 3. Reduction in inhomogeneous broadening due to dual resonance: (a) Bottom panel: Spatial potential fluctuation due to inhomogeneity in the system (external + internal). Top panel: The resulting spatial fluctuation in the exciton energy (shaded curve). The intersections with the solid lines are the equienergy spots at three different exciton energies (marked 1–3). (b) Schematic description of the inhomogeneous PL broadening reduction obtained by single-step scattering with the A'_1 phonon mode due to dual resonance. The bottom inset schematically shows the spatial profile of the equienergy spots at three different $1s$ exciton emission energies [marked as 1–3 in (a)]. (c) Left panel: PL broadening due to light emission from all the energy states (spots) in the distribution. Right panel: PL linewidth narrowing due to emission from specific $1s$ energy states resulting from narrow resonance in single-step relaxation. (d) Experimental result of single-step relaxation through A'_1 phonon mode (M3 process) in orange shaded curves, resulting in the sharp $1s$ exciton peak. The excitation wavelength is tuned such that the emission line scans through the inhomogeneously broadened PL emission peak (M1 process). The latter is obtained by off-resonant 532 nm excitation (raw emission data in gray trace and fitting in black dashed trace). (e) Spatial imaging from $1s$ emission highlighting the change in the spatial distribution of the equienergy spots at different exciton emission energies [marked by arrows in (e)]. The corresponding excitation wavelengths are indicated in the insets. (f) A linewidth of $\sim 0.19 \pm 0.07$ meV is obtained on deconvoluting the exciton spectrum (in symbols) with the excitation laser having nonzero broadening (in yellow shading). The fitted curve after deconvolution (in solid trace) is also shown.

the standard deviation to mean ratio reducing from 8% under off-resonant excitation to 3% with this technique.

V. ENHANCED QUANTUM EFFICIENCY IN SPITE OF FLG ENCAPSULATION

The internal quantum efficiency of emission in the proposed mechanism can be written as a product of relaxation (η_{rel}) and emission (η_{em}) quantum efficiency:

$$\eta_{\text{int}} = \underbrace{\frac{\gamma_{\text{res}}}{\gamma_{\text{res}} + \gamma_{\text{off}-\text{res}} + \gamma_{\text{gr}}}}_{\eta_{\text{rel}}} \underbrace{\frac{\gamma_{\text{r}}}{\gamma_{\text{r}} + \gamma_{\text{nr}} + \gamma_{\text{gr}}}}_{\eta_{\text{em}}}. \quad (1)$$

As a result of the ultrafast relaxation rate (γ_{res}) in M3: (1) The generated oscillator strength is primarily transferred to the resonating final $1s$ states. This avoids the distribution of the oscillator strength among other inhomogeneously distributed states, like in the case of other relaxation processes such as M1 ($\gamma_{\text{off}-\text{res}}$). (2) The loss due to exciton transfer to the top and bottom FLG (γ_{gr}) during such fast relaxation is also minimized. Therefore, as $\gamma_{\text{res}} \gg \gamma_{\text{off}-\text{res}}$ and γ_{gr}, the generated oscillator strength efficiently relaxes from the ns band to the $1s$ band due to dual resonance, thus making η_{rel} large. This

is evident in Fig. 2(d) by the large ratio of the intensity of the green curve (M3) to the pink background (M1). γ_{r} and γ_{nr} represent the exciton radiative and nonradiative (other than exciton transfer to FLG) decay rates once it relaxes to the $1s$ band. For simplicity, we assumed that γ_{gr} is energy independent in Eq. (1).

VI. HIGH EXCITON VALLEY POLARIZATION AND VALLEY COHERENCE

Excitons inherit the angular momentum of the electronic bands in the K, K' valleys. Therefore, an incoming circularly (linearly) polarized light generates excitons in a specific valley (superposition state of both the valleys) [28–30]. During (1) the relaxation process, and (2) inside the light cone, the degradation in the exciton valley polarization/coherence occurs due to a coupled effect of exciton scattering and pseudospin precession due to exchange interaction [19,31] [Fig. 4(a)]. In addition, during the relaxation process M1, the scattering with multiple phonons with different polarizations may also lead to a random phase accumulation. We observe these effects by the gradual improvement in the exciton DOLP, for the broad background peak (in pink) in Figs. 2(d)–2(f), as the incoming
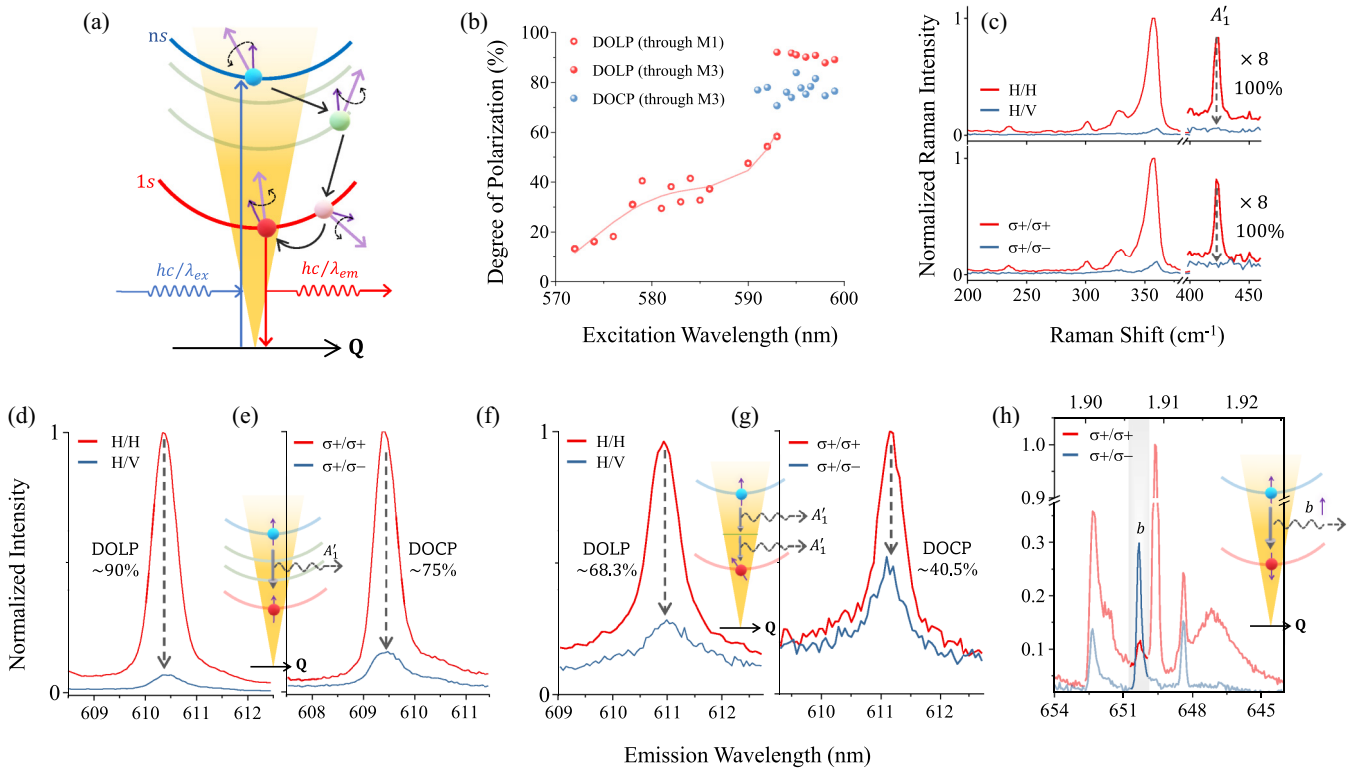
FIG. 4. Polarization control during single-step relaxation: (a) During relaxation mechanism M1 and inside the light cone, the polarization degrades due to scattering coupled with pseudospin (dark purple arrow) precession around the exchange induced magnetic field (light purple arrow). (b) DOLP (in red) of the $1s$ exciton peak that forms after relaxation mechanism M1 [open red circles, obtained from pink background in Figs. 2(d)–2(f)] and M3 [solid red circles, obtained from green shaded peaks in Figs. 2(d)–2(f)] is shown. The DOCP of the excitons formed after M3 relaxation process is also shown (solid blue circles). (c) Polarization resolved Raman spectrum of WS$_2$ in the GWG stack (532 nm excitation). The A_1' phonon peak is fully polarized, indicating that the polarization of the incoming light is retained on scattering with the A_1' phonons. (d,e) The result of single-step scattering with the A_1' phonons leads to the observation of high (d) DOLP and (e) DOCP in the GWG stack. Inset: A schematic view of the mechanism. (f), (g) The degradation in (f) DOLP and (g) DOCP due to scattering with the $2A_1'$ phonon mode. Inset: A schematic view of the mechanism. (h) Single-step scattering with a chiral phonon mode (b) leads to polarization reversal of the incoming light in the FLG-MoS$_2$-FLG stack (highlighted by gray shading). Inset: A schematic view of the mechanism.

excitation is tuned closer to the $1s$ resonance [open red circles in Fig. 4(b)].

The FLG encapsulation in the GWG sample helps to suppress both these effects. First, in mechanism M3, as we selectively choose the phonon mode that dominates the single-step relaxation, the uncontrolled pseudospin randomization during the relaxation process is avoided. For example, the polarization of the incoming light does not change by scattering with the A_1' phonon mode due to the diagonal form of its Raman tensor [32,33] [schematically depicted in the inset of Figs. 4(d) and 4(e)]. This is depicted by the fully polarized A_1' Raman peak in Fig. 4(c) [top (bottom) panel for linear (circular) polarization] as obtained using 532 nm excitation. Hence, when we achieve a resonance with the A_1' mode in the exciton relaxation process, in Fig. 4(b), we observe a negligible change in the exciton DOLP (red solid symbols) and DOCP (blue solid symbols) on varying λ_{ex}. Second, once the exciton relaxes down to the $1s$ light cone, the FLG encapsulation helps to preserve the polarization inside the light cone by (a) reducing pseudospin precession frequency due to screening induced suppression of the exchange interaction,

and (b) reducing the exciton lifetime due to fast charge transfer to FLG [19]. As a combined effect, we observe a DOLP of ~90% and a DOCP of ~75% of $1s$ excitons in the GWG stack [Figs. 4(d) and 4(e)].

On the other hand, when the $2A_1'$ phonon mode dominates the relaxation process, we obtain a degraded DOLP (DOCP) of ~68.3% (~40%) [Figs. 4(f) and 4(g)]. This suggests that the additional exchange interaction in the intermediate state between the two consecutive scattering events during the relaxation results in the observed polarization degradation, as schematically shown in the inset of Figs. 4(f) and 4(g). This technique can also tune the exciton polarization strategically during the relaxation process if we choose the appropriate phonon mode. For example, during the exciton-phonon scattering, complete reversal of the incoming polarization is possible on resonating with a chiral phonon mode, to ensure angular momentum conservation in a C_{3h} symmetric system [schematically depicted in the inset of Fig. 4(h)]. We observe such reversal using the chiral "b" phonon mode [34–37] at 420 cm^{-1} in a FLG-MoS$_2$-FLG sample, upon resonating with which, the outgoing photon is reverse circularly polarized with respect to the incoming circular polarization [Fig. 4(h)].
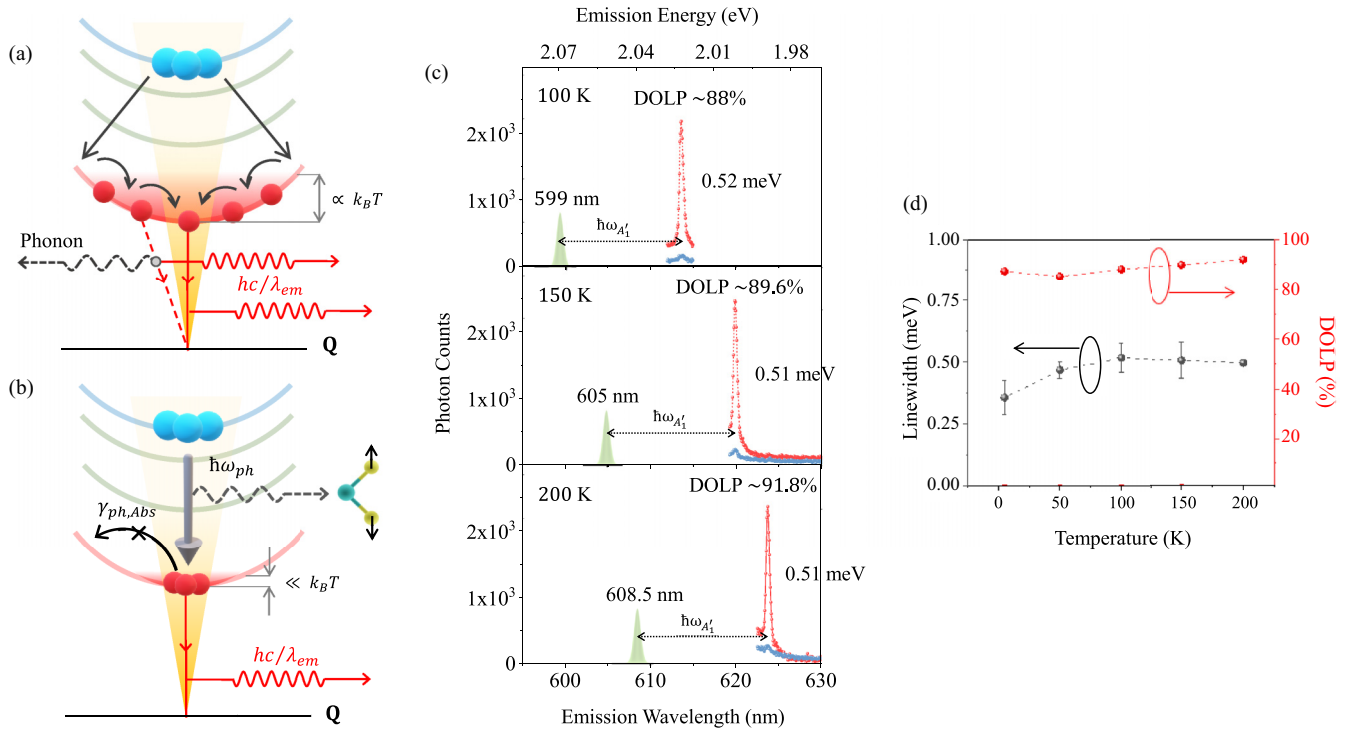
FIG. 5. Temperature independent ultranarrow, highly polarized exciton peaks: (a) The exciton population distribution broadens with $k_B T$ during relaxation mechanism M1. This causes linewidth broadening due to enhanced (phonon assisted) contribution from the higher $|\mathbf{Q}|$ states outside the light cone. The higher $|\mathbf{Q}|$ states are also long lived and experience larger exchange, leading to polarization degradation. (b) The population distribution is mainly limited within the light cone through relaxation mechanism M3. (c) Representative linear polarization resolved emission spectra at 100, 150, and 200 K, obtained after single-step relaxation with the A_1' phonon. The DOLP and deconvoluted linewidth values are shown in the insets. (d) The extracted $1s$ exciton PL linewidth (in black symbols) and the DOLP (in red symbols) as a function of temperature.

VII. TEMPERATURE ROBUST EXCITON LINEWIDTH AND POLARIZATION

When sample temperature increases, upon relaxation through mechanism M1, the states outside the light cone get populated and start contributing to light emission mediated by phonons [Fig. 5(a)]. These momentum-dark states are long lived, which give sufficient time to the exciton population to achieve thermal equilibrium before radiative recombination. This enhances the homogeneous linewidth with $k_B T$ [38,39].

In the current technique, direct light cone to light cone transition happens from the higher energy band to the $1s$ band. Therefore, the excitons directly relax to the lowest energy states in the $1s$ band at all temperatures. As γ_r and γ_{gr} ($\gg \gamma_{nr}$) are independent of temperature, the overall exciton lifetime ($\tau \sim \frac{1}{\gamma_r + \gamma_{gr}}$) inside the light cone remains temperature independent in this process. Since the phonon absorption process ($\gamma_{ph,Abs}$) is much slower than the net exciton decay rate (i.e., $\gamma_{ph,Abs} \ll \gamma_r + \gamma_{gr}$), the excitons can hardly move outside the light cone. Consequently, the excitons do not have enough time to attain thermal equilibrium before radiative recombination [Fig. 5(b)]. Therefore, because of this nonequilibrium exciton population inside the light cone, we observe a relatively weak influence of temperature on the linewidth through this technique [Figs. 5(c) and 5(d)] – a key aspect of this work.

Exciton polarization degrades with temperature when it relaxes by mechanism M1, because of two primary reasons: (1) *enhancement in the overall phonon scattering rate* – as more phonon modes start participating in the exciton relaxation process, the random phase accumulation during relaxation increases with temperature; and (2) *enhanced contribution of excitons outside the light cone* – as explained previously, the fractional contribution of excitons outside the light cone increases with temperature due to relaxation mechanism M1 [Fig. 5(a)]. This in turn has two effects on polarization degradation. First, the net exchange interaction (J) increases with the exciton center of mass momentum ($\mathbf{Q}$) as $J \propto -V(\mathbf{Q})|\mathbf{Q}|^2$ where $V(\mathbf{Q})$ is the electron-hole Coulomb interaction [40]. This leads to a faster pseudospin dephasing for excitons with larger $|\mathbf{Q}|$. Second, the excitons outside the light cone being momentum dark, are long-lived, and hence suffer from more accumulation of random phase in the pseudospin vector. In the proposed technique, by minimizing all these processes through relaxation process M3, we observe a dramatically negligible influence of temperature on the exciton valley coherence [Figs. 5(c) and 5(d)].

VIII. DISCUSSION

Apart from $1s$ emission, the resonant Raman scattered photons also energetically coincide with the emitted light,

and often it becomes challenging to segregate these two mechanisms [41,42]. While the emission process is a result of a cascade of photon absorption, relaxation through exciton-phonon scattering, and photon emission through recombination of the 1s exciton, the resonant Raman process is an instantaneous process maintaining coherence. We argue that the 1s excitonic emission has the dominant contribution over resonant Raman scattering in the current scenario of dual resonance based on the following observations: (a) We note a significantly lower than 100% DOCP and DOLP in the light output [Figs. 4(d)–4(g)], while the pure Raman process should yield 100% degree of polarization [see, for example, Fig. 4(c)] for A_1' and $2A_1'$ modes possessing a diagonal Raman tensor. (b) The light output has DOCP < DOLP in Figs. 4(d)–4(g), which is a characteristic of 2D exciton emission due to the in-plane nature of the pseudomagnetic field generated by the exchange interaction. (c) The strong correlation between the spectral feature of the nonresonant 1s exciton emission and the envelope of the output under dual resonance when the excitation wavelength is tuned [Fig. 3(d)] suggests the key role played by the 1s state in the process, which should not happen for Raman scattering. (d) Strikingly, when the emission quantum efficiency is suppressed by increasing the number of layers of WS$_2$, the output photon count becomes independent of the spectral feature of the 1s state, indicating a Raman scattering dominated process for few layers (details in Note S2 in Supplemental Material [22]). (e) We also observe a dramatic reduction in the peak intensity in the few-layer WS$_2$ samples. Being an instantaneous process, if resonant Raman scattering would have dominated the peak in the monolayer, we would expect similar intensity in few-layer samples as well, suggesting the peak intensity is dominated by excitonic emission in monolayer. (f) The noticeable linewidth difference between the excitation laser and the emission peak [Fig. 3(f)] is not observed for the A_1' Raman peak obtained with off-resonant excitation in the GWG stack, in which case the Raman linewidth closely matches the linewidth of the excitation laser (see Note S2 in Supplemental Material [22]).

Due to protective encapsulation by FLG and the intrinsic nature of narrow resonance, we find the emission features from the sample to remain robust for a long time (see representative data taken on the same stack after 2 months in Fig. S7 in Supplemental Material [22]). The strength of the proposed technique lies in obtaining the narrowest excitonic peak reported to date even in the presence of sample inhomogeneity – allowing us to achieve close to the true homogeneous linewidth in the sample. This can help experiments (including Stark effect, Zeeman splitting, Rabi splitting) where the observation of a small excitonic peak shift is usually obscured due to a large linewidth. The sharpness of the peak along with the observed high degree of exciton polarization is robust even at higher temperatures – making the technique promising for several experiments which earlier required cryogenic temperature to achieve these features. The combination of enhanced quantum efficiency, narrow linewidth, high degree of valley polarization and coherence, and the robustness of these features against sample age and temperature makes the proposed technique powerful to obtain a near-ideal atomically thin light emitter.

IX. METHODS

A. Sample preparation

To prepare the GWG stack, the material is first exfoliated on a polydimethylsiloxane (PDMS) sheet. After locating an appropriate flake, it is transferred on a Si substrate covered with 285 nm thick thermally grown SiO$_2$, one flake at a time. The thickness of the bottom and the top graphene is 2–3 nm. The sample is annealed at 200 °C for 5 h (pressure $\sim10^{-6}$ Torr) to ensure good adhesion between successive layers.

B. Measurement details

All the measurements are taken in a closed-cycle optical cryostat (Montana Instruments) at 5 K using a 50× long working distance objective having a numerical aperture of 0.5. The photoluminescence excitation measurement is carried out using a supercontinuum laser source (NKT Photonics). The output of the laser is passed through an acousto-optic tunable filter (AOTF) followed by one or two monochromators (Edmund Optics) to ensure spectrally narrow excitation pulses. In all the wavelength dependent measurements, the excitation wavelength is tuned by a step of 1 nm. All measurements except the narrowest emission linewidth measurements were taken with one monochromator. The laser linewidth with one monochromator is $\sim$1.2 meV. The narrowest exciton linewidth measurements (in Fig. 3(f) and Figs. S6 and S7 in Supplemental Material [22]) were obtained using two monochromators in cascade. The laser linewidth with two monochromators is $\sim$0.8 meV. A 610 nm bandpass filter is kept in the detection side to monitor 1s exciton emission. The average power used for the measurements in this work is <5 µW. Linear polarization resolved measurements are carried out by using a half-wave plate (analyzer) in the emission (detection) side. DOLP [= $(I_{H/H} - I_{H/V})/(I_{H/H} + I_{H/V})$] is obtained by keeping the incoming polarization in the parallel ($I_{H/H}$) and perpendicular ($I_{H/V}$) directions with respect to the analyzer. For the circular polarization resolved measurements, an additional quarter-wave plate is inserted right before the objective lens. DOCP [= $(I_{\sigma+/\sigma+} - I_{\sigma+/\sigma-})/(I_{\sigma+/\sigma+} + I_{\sigma+/\sigma-})$] is obtained by changing the incoming linear polarization direction from +45° to −45° with the fast axis of the quarter-wave plate. For temperature dependent measurements, the excitation wavelength is tuned to ensure single-step resonance with the A_1' phonon mode at each temperature.

Data available on reasonable request from the corresponding author.

[1] K. F. Mak, C. Lee, J. Hone, J. Shan, and T. F. Heinz, Phys. Rev. Lett. **105**, 136805 (2010).

[2] A. Splendiani, L. Sun, Y. Zhang, T. Li, J. Kim, C. Y. Chim, G. Galli, and F. Wang, Nano Lett. **10**, 1271 (2010).

[3] J. S. Ross, S. Wu, H. Yu, N. J. Ghimire, A. M. Jones, G. Aivazian, J. Yan, D. G. Mandrus, D. Xiao, W. Yao, and X. Xu, Nat. Commun. **4**, 1474 (2013).

[4] I. Epstein, B. Terrés, A. J. Chaves, V. Pusapati, D. A. Rhodes, B. Frank, V. Zimmermann, Y. Qin, K. Watanabe, T. Taniguchi, H. Giessen, S. Tongay, J. C. Hone, N. M. R. Peres, and F. H. L. Koppens, Nano Lett. **20**, 3545 (2020).

[5] Y. Cho and T. C. Berkelbach, Phys. Rev. B **97**, 041409 (2018).

[6] A. Raja, L. Waldecker, J. Zipfel, Y. Cho, S. Brem, J. D. Ziegler, M. Kulig, T. Taniguchi, K. Watanabe, E. Malic, T. F. Heinz, T. C. Berkelbach, and A. Chernikov, Nat. Nanotechnol. **14**, 832 (2019).

[7] K. Zhang, S. Feng, J. Wang, A. Azcatl, N. Lu, R. Addou, N. Wang, C. Zhou, J. Lerach, V. Bojan, M. J. Kim, L. Chen, R. M. Wallace, M. Terrones, J. Zhu, and J. A. Robinson, Nano Lett. **15**, 6586 (2015).

[8] D. Edelberg, D. Rhodes, A. Kerelsky, B. Kim, J. Wang, A. Zangiabadi, C. Kim, A. Abhinandan, J. Ardelean, M. Scully, D. Scullion, L. Embon, R. Zu, E. J. G. Santos, L. Balicas, C. Marianetti, K. Barmak, X. Zhu, J. Hone, and A. N. Pasupathy, Nano Lett. **19**, 4371 (2019).

[9] W. Zhou, X. Zou, S. Najmaei, Z. Liu, Y. Shi, J. Kong, J. Lou, P. M. Ajayan, B. I. Yakobson, and J. C. Idrobo, Nano Lett. **13**, 2615 (2013).

[10] J. Hong, Z. Hu, M. Probert, K. Li, D. Lv, X. Yang, L. Gu, N. Mao, Q. Feng, L. Xie, J. Zhang, D. Wu, Z. Zhang, C. Jin, W. Ji, X. Zhang, J. Yuan, and Z. Zhang, Nat. Commun. **6**, 6293 (2015).

[11] H. Y. Jeong, Y. Jin, S. J. Yun, J. Zhao, J. Baik, D. H. Keum, H. S. Lee, and Y. H. Lee, Adv. Mater. **29**, 1605043 (2017).

[12] G. Moody, C. K. Dass, K. Hao, C. Chen, L. Li, A. Singh, K. Tran, G. Clark, X. Xu, G. Berghauser, E. Malic, A. Knorr, and X. Li, Nat. Commun. **6**, 8315 (2015).

[13] O. A. Ajayi, J. V. Ardelean, G. D Shepard, J. Wang, A. Antony, T. Taniguchi, K. Watanabe, T. F. Heinz, S. Strauf, X. Zhu, and J. C. Hone, 2D Mater. **4**, 031011 (2017).

[14] S. Shree, M. Semina, C. Robert, B. Han, T. Amand, A. Balocchi, M. Manca, E. Courtade, X. Marie, T. Taniguchi, K. Watanabe, M. M. Glazov, and B. Urbaszek, Phys. Rev. B **98**, 035302 (2018).

[15] S. Hayashida, R. Saitoh, K. Watanabe, T. Taniguchi, K. Sawano, and Y. Hoshi, ACS Appl. Electron. Mater. **2**, 2739 (2020).

[16] F. Cadiz, E. Courtade, C. Robert, G. Wang, Y. Shen, H. Cai, T. Taniguchi, K. Watanabe, H. Carrere, D. Lagarde, M. Manca, T. Amand, P. Renucci, S. Tongay, X. Marie, and B. Urbaszek, Phys. Rev. X **7**, 021026 (2017).

[17] T. Hotta, A. Ueda, S. Higuchi, M. Okada, T. Shimizu, T. Kubo, K. Ueno, T. Taniguchi, K. Watanabe, and R. Kitaura, ACS Nano **15**, 1370 (2021).

[18] E. Lorchat, L. E. P. López, C. Robert, D. Lagarde, G. Froehlicher, T. Taniguchi, K. Watanabe, X. Marie, and S. Berciaud, Nat. Nanotechnol. **15**, 283 (2020).

[19] G. Gupta, K. Watanabe, T. Taniguchi, and K. Majumdar, Light Sci. Appl. **12**, 173 (2023).

[20] A. Raja, A. Chaves, J. Yu, G. Arefe, H. M. Hill, A. F. Rigosi, T. C. Berkelbach, P. Nagler, C. Schuller, T. Korn, C. Nuckolls, J. Hone, L. E. Brus, T. F. Heinz, D. R. Reichman, and A. Chernikov, Nat. Commun. **8**, 15251 (2017).

[21] G. Gupta, S. Kallatt, and K. Majumdar, Phys. Rev. B **96**, 081403 (2017).

[22] See Supplemental Material at http://link.aps.org/supplemental/10.1103/PhysRevB.108.075436 for the calculation details of exciton eigenenergy spectrum, distinguishing excitonic resonance from the resonant Raman process, linear polarization resolved PL spectrum at different excitation wavelengths, deconvoluted linewidth as a function of the excitation wavelength, single-step resonance results from a different GWG sample, PL spectrum showing the narrow linewidth, and measurement taken on the GWG sample after two months of sample preparation.

[23] M. R. Molas, K. Nogajewski, M. Potemski, and A. Babiński, Sci. Rep. **7**, 5036 (2017).

[24] M. Zinkiewicz, K. Nogajewski, M. Bartos, K. Watanabe, T. Taniguchi, M. Potemski, A. Babiński, and M. R. Molas, Acta Phys. Pol. A **136**, 624 (2019).

[25] H. H. Fang, B. Han, C. Robert, M. A. Semina, D. Lagarde, E. Courtade, T. Taniguchi, K. Watanabe, T. Amand, B. Urbaszek, M. M. Glazov, and X. Marie, Phys. Rev. Lett. **123**, 067401 (2019).

[26] T. Jakubczyk, K. Nogajewski, M. R. Molas, M. Bartos, W. Langbein, M. Potemski, and J. Kasprzak, 2D Mater. **5**, 031007 (2018).

[27] C. Ferrante, G. Di Battista, L. E. Parra Lopez, G. Batignani, E. Lorchat, A. Virga, S. Berciaud, and T. Scopignod, Proc. Natl. Acad. Sci. USA **119**, e2119726119 (2022).

[28] T. Cao, G. Wang, W. Han, H. Ye, C. Zhu, J. Shi, Q. Niu, P. Tan, E. Wang, B. Liu, and J. Feng, Nat. Commun. **3**, 887 (2012).

[29] K. F. Mak, K. He, J. Shan, and T. F. Heinz, Nat. Nanotechnol. **7**, 494 (2012).

[30] A. M. Jones, H. Yu, N. J. Ghimire, S. Wu, G. Aivazian, J. S. Ross, B. Zhao, J. Yan, D. G. Mandrus, D. Xiao, W. Yao, and X. Xu, Nat. Nanotechnol. **8**, 634 (2013).

[31] M. Z. Maialle, E. A. De Andrada, E. Silva, and L. J. Sham, Phys. Rev. B **47**, 15776 (1993).

[32] Y. Zhao, S. Zhang, Y. Shi, Y. Zhang, R. Saito, J. Zhang, and L. Tong, ACS Nano **14**, 10527 (2020).

[33] B. Miller, J. Lindlau, M. Bommert, A. Neumann, H. Yamaguchi, A. Holleitner, A. Högele, and U. Wurstbauer, Nat. Commun. **10**, 807 (2019).

[34] R. Yoshizaki, K. Uchinokura, T. Nakashizu, and E. Matsuura, J. Phys. Soc. Jpn. **53**, 811 (1984).

[35] T. Livneh and E. Sterer, Phys. Rev. B **81**, 195209 (2010).

[36] B. Chakraborty, H. S. S. R. Matte, A. K. Sood, and C. N. R. Rao, J. Raman Spectrosc. **44**, 92 (2013).

[37] K. Gołasa, M. Grzeszczyk, R. Bozek, P. Leszczyński, A. Wysmołek, M. Potemski, and A. Babiński, Solid State Commun. **197**, 53 (2014).

[38] J. Feldmann, G. Peter, E. O. Göbel, P. Dawson, K. Moore, C. Foxon, and R. J. Elliott, Phys. Rev. Lett. **59**, 2337 (1987).

[39] S. A. Lyon, J. Lumin. **35**, 121 (1986).

[40] H. Yu, G. Bin Liu, P. Gong, X. Xu, and W. Yao, Nat. Commun. **5**, 3876 (2014).

[41] Y. R. Shen, Phys. Rev. B **9**, 622 (1974).

[42] Peter Y. Yu and M. Cardona, *Fundamentals of Semiconductors* (Springer Science & Business Media, Berlin, 2010).